

Dual thermal pseudocritical features in a spin-1/2 Ising chain with twin-diamond geometry

Onofre Rojas

*Department of Physics, Institute of Natural Science,
Federal University of Lavras, Lavras, MG, Brazil*

We study the coupled twin-diamond chain, a decorated one-dimensional Ising model motivated by the magnetic structure of $\text{Cu}_2(\text{TeO}_3)_2\text{Br}_2$. By applying an exact mapping to an effective Ising chain, we obtain the full thermodynamic description of the system through a compact transfer-matrix formulation. The ground-state analysis reveals five distinct phases, including two frustrated sectors with extensive degeneracy. These frustrated regions give rise to characteristic entropy plateaus and separate the ordered phases in the zero-temperature diagram. At low temperatures the model exhibits peculiar sharp yet continuous variations of entropy, magnetization, and response functions, reflecting clear signatures of pseudotransition behavior. The coupled twin-diamond chain thus provides an exactly solvable setting in which competing local configurations and internal frustration lead to pronounced dual pseudocritical features in one dimension.

I. INTRODUCTION.

One-dimensional lattice models have recently attracted renewed attention because certain systems display thermodynamic anomalies that closely resemble finite-temperature phase transitions [1–3]. These anomalies, known as pseudotransitions, differ from genuine criticality even though they reproduce several of its characteristic signatures. First derivatives of the free energy, such as entropy and magnetization, exhibit steep but continuous variations near a pseudocritical temperature, while second derivatives, including the specific heat and magnetic susceptibility, develop sharp yet finite peaks [4]. Numerical and analytical studies of decorated Ising and Ising-Heisenberg chains have further shown that these pseudotransitions can mimic essential features of critical phenomena: the correlation length increases rapidly near the pseudocritical temperature [5], and several response functions follow power-law forms governed by a universal set of pseudocritical exponents identified in many one-dimensional decorated models [6].

Peculiar decorated one-dimensional spin models provide a natural framework for these anomalies because their internal degrees of freedom generate competing low-energy sectors whose exchange of dominance at a characteristic temperature produces fully analytic yet remarkably sharp thermodynamic crossovers. This mechanism has been identified in several exactly solvable systems, including the Ising-XYZ diamond chain, where quasi-phases and pseudotransitions were first clearly characterized [4, 5], the coupled spin-electron double-tetrahedral chain, which exhibits frustration-enhanced entropy plateaus [1], and various Ising-Heisenberg ladders and tubes that display pseudocritical behavior governed by universal exponents [2, 6–10]. A unified interpretation based on the decoration-iteration mapping clarified that the anomalous crossover originates from temperature-dependent effective couplings and effective fields generated after integrating out the decorated sublattices [6]. Furthermore, subsequent analyses estab-

lished that the residual entropy at zero-temperature phase boundaries serves as a reliable predictor for the appearance of pseudotransitions in decorated chains [11].

Pseudotransition behavior is not restricted to decorated chains. Several strictly one-dimensional models without auxiliary spins or internal bond structures also display sharp thermal crossovers when their parameters are tuned to generate competing low-energy configurations. A notable example is the extended Hubbard model at half filling in the atomic limit, where pronounced thermodynamic anomalies mimic those associated with quasi-phases [12]. A similar crossover between antiferromagnetic and charge-ordered configurations was reported in a minimal spin-pseudospin description of cuprate chains, accompanied by a strong but finite specific heat peak [13]. Related effects occur in frustrated Potts-type models such as the q -state Potts-Zimm-Bragg formulation [14], in dilute Ising chains with impurity induced frustration [15], and in water-like lattice models incorporating van der Waals interactions and directional bonding [16]. These examples demonstrate that the essential ingredients behind pseudotransitions, namely competing sectors with small energy gaps and enhanced degeneracies, can arise naturally even in purely one-dimensional systems without explicit decoration.

Diamond chain geometries play a central role in several magnetic compounds, which explains why diamond chain models have been extensively studied in the theoretical literature [3, 17–19]. A prominent example is the natural mineral azurite $\text{Cu}_3(\text{CO}_3)_2(\text{OH})_2$ [20, 21], whose magnetic properties motivated detailed analyses of spin 1/2 Ising and Ising-Heisenberg diamond chains. Other compounds, such as the mixed valent iron diamond chain with single ion anisotropy [22], further support the idea that the diamond motif is an efficient source of frustration and anomalous thermodynamic behavior in one dimensional systems, among other similar structures [7, 23, 24]. For these reasons, diamond chains remain key reference models for exploring the origin of entropy plateaus, degeneracy driven anomalies, and pseudocritical behavior

in one dimension.

Beyond simple diamond chains, an increasing number of materials display coupled diamond like building blocks, often arranged in layers or extended structural networks. A representative case is the oxohalide $\text{Cu}_2(\text{TeO}_3)_2\text{Br}_2$, where Cu^{2+} ions form diamond shaped units that are connected along a crystallographic direction [25]. Similar motifs appear in more complex families such as the $\text{CuO-CuCl}_2\text{-SeO}_2$ series [26], as well as in the oxohalides $\text{Cu}_3(\text{SeO}_3)_2\text{Cl}_2$ and $\text{Cu}_3(\text{TeO}_3)_2\text{Br}_2$ [27], and the insulating spin-gap compound $\text{CdCu}_2(\text{SeO}_3)_2\text{Cl}_2$ [28]. Such structural features strongly motivate the study of theoretical models that incorporate more than one diamond unit per cell. The coupled twin diamond chain examined in the present work represents the minimal extension capable of capturing this additional connectivity and allows us to investigate how the interaction between two diamond units within each cell can produce multiple frustrated sectors and distinct pseudocritical features in a single exactly solvable framework.

In the present work, the coupled twin-diamond chain is therefore introduced as a minimal theoretical model inspired by such diamond-based magnetic structures[25], rather than as a quantitative description of any specific compound. The central novelty of the coupled twin-diamond chain lies in the fact that its minimal unit cell supports more than one frustrated low-energy manifold with different extensive degeneracies. As a result, the system exhibits two well-separated pseudocritical temperature scales associated with successive entropy-driven crossovers between competing configurations. This provides a clean exactly solvable example in which dual pseudotransition features arise within a single one-dimensional decorated Ising geometry, rather than from tuning parameters between distinct models. We further show that these features remain robust even when the two spin sublattices respond differently to an external magnetic field.

This work is organized as follows. Sect. II introduces the Hamiltonian, outlines the transfer-matrix solution, and presents the zero-temperature phase diagram together with the corresponding pseudotransition features. Sect. III examines the thermodynamic behavior in the anomalous region where these pseudotransitions emerge. Finally, Sec. IV summarizes the main conclusions.

II. COUPLED TWIN-DIAMOND CHAIN MODEL

In this section we consider a coupled twin-diamond chain (CTDC) inspired by the compound $\text{Cu}_2(\text{TeO}_3)_2\text{Br}_2$ whose magnetic structure consists of spin-1/2 Cu^{2+} ions arranged in diamond-like units[25]. Here we assume the simplest case that the magnetic interactions are purely of the Ising type. A schematic representation of the lattice geometry is shown in Fig. 1. Blue spheres denote the nodal spins, whereas black spheres indicate the two spins

forming each internal dimer.

Each unit cell of the CTDC contains a nodal Ising spin s_k and a pair of Ising spins $S_{a,k}$ and $S_{b,k}$. The local fields acting on the two types of spins may differ because the corresponding gyromagnetic factor for nodal spins g_0 and dimer spins g_1 . The resulting Zeeman terms are $h_0 = \mu_B g_0 B$ and $h_1 = \mu_B g_1 B$, which act on the nodal and dimer spins, respectively.

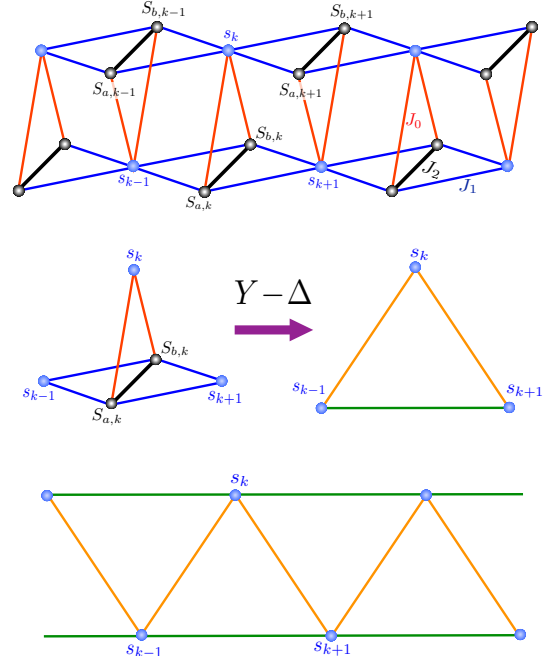


Figure 1: (Top) Schematic representation of the spin-1/2 CTDC. Black spheres denote dimer spins ($S_{a,k}$ and $S_{b,k}$), while blue spheres represent nodal Ising spins. Blue (red) lines indicate the couplings between dimer and nodal spins, associated with the exchange interactions J_1 (J_0), respectively, whereas the black line corresponds to the intra-dimer exchange interaction (J_2). (Middle) Illustration of the star-triangle transformation. (Bottom) Resulting effective spin chain with nearest- and next-nearest-neighbor interactions.

A. Hamiltonian and transfer matrix

The Hamiltonian of the coupled twin-diamond Ising chain reads

$$\mathcal{H} = \sum_{k=1}^N \{ [J_0 s_k + J_1 (s_{k-1} + s_{k+1})] (S_{a,k} + S_{b,k}) + J_2 S_{a,k} S_{b,k} - h_1 (S_{a,k} + S_{b,k}) - h_0 s_k \}. \quad (1)$$

Here J_2 is the intra-dimer coupling, J_0 couples the nodal spin s_k to the adjacent dimer, and J_1 couples the dimer to the neighboring nodal spins s_{k-1} and s_{k+1} along the chain. Due to $g_0 \neq g_1$ in general, the two sublattices respond differently to the same external magnetic field

B. The Hamiltonian (1) is invariant under the exchange $S_{a,k} \leftrightarrow S_{b,k}$ and is translationally invariant along the chain.

At this stage, the internal dimer spins $S_{a,k}$ and $S_{b,k}$ can be eliminated by means of a local star-triangle transformation [29–31], as schematically illustrated in Fig. 1 (middle). For fixed values of the neighboring nodal spins, the Boltzmann weight of each decorated cell is obtained by explicitly summing over the dimer degrees of freedom. The repeated application of this mapping along the chain yields an effective one-dimensional Ising model for the nodal spins, with temperature-dependent nearest- and next-nearest-neighbor interactions and an effective field.

The resulting effective model can be treated exactly by the transfer-matrix method. Because the mapping generates next-nearest-neighbor couplings, the transfer matrix \mathbf{V} acts on pairs of adjacent nodal spins and therefore has dimension 4×4 . Analogous to the transfer matrix of the extended Ising chain [32], \mathbf{V} is written in the pair basis $\{|+, +\rangle, |+, -\rangle, |-, +\rangle, |-, -\rangle\}$ as

$$\mathbf{V} = \begin{pmatrix} \mathbf{r} & \mathbf{m} & 0 & 0 \\ 0 & 0 & \mathbf{p} & \mathbf{n} \\ \mathbf{m} & \mathbf{q} & 0 & 0 \\ 0 & 0 & \mathbf{n} & \mathbf{t} \end{pmatrix}, \quad (2)$$

where the basis states are labeled by the nodal-spin pairs (s_k, s_{k+1}) . The matrix elements \mathbf{r} , \mathbf{m} , \mathbf{p} , \mathbf{n} , \mathbf{q} , \mathbf{t} incorporate the local Boltzmann weights for the four possible configurations of neighboring nodal spins and the internal dimer

$$\mathbf{r} = 2e^{-\frac{J_2+2h_0}{4k_B T}} \cosh\left(\frac{J_0+2J_1+h_1}{k_B T}\right) + 2e^{\frac{J_2-2h_0}{4k_B T}}, \quad (3)$$

$$\mathbf{m} = 2e^{-\frac{3J_2+2h_0}{12k_B T}} \cosh\left(\frac{J_0+h_1}{k_B T}\right) + 2e^{\frac{3J_2-2h_0}{12k_B T}}, \quad (4)$$

$$\mathbf{p} = 2e^{-\frac{3J_2+2h_0}{12k_B T}} \cosh\left(\frac{2J_1-J_0+h_1}{T}\right) + 2e^{\frac{3J_2-2h_0}{12k_B T}}, \quad (5)$$

$$\mathbf{n} = 2e^{-\frac{3J_2-2h_0}{12k_B T}} \cosh\left(\frac{J_0-h_1}{k_B T}\right) + 2e^{\frac{3J_2+2h_0}{12k_B T}}, \quad (6)$$

$$\mathbf{q} = 2e^{-\frac{3J_2-2h_0}{12k_B T}} \cosh\left(\frac{2J_1-J_0-h_1}{k_B T}\right) + 2e^{\frac{3J_2+2h_0}{12k_B T}}, \quad (7)$$

$$\mathbf{t} = 2e^{-\frac{J_2-2h_0}{4k_B T}} \cosh\left(\frac{2J_1+J_0-h_1}{k_B T}\right) + 2e^{\frac{J_2+2h_0}{4k_B T}}, \quad (8)$$

The eigenvalues $\lambda_i (i = 1, \dots, 4)$ follow from the secular equation $\det(\mathbf{V} - \lambda I) = 0$, which yields a quartic polynomial

$$\lambda^4 + \mathbf{c}_3 \lambda^3 + \mathbf{c}_2 \lambda^2 + \mathbf{c}_1 \lambda + \mathbf{c}_0 = 0, \quad (9)$$

where the coefficients are given by

$$\mathbf{c}_0 = -(\mathbf{q}\mathbf{r} - \mathbf{m}^2)(\mathbf{p}\mathbf{t} - \mathbf{n}^2) < 0, \quad (10)$$

$$\mathbf{c}_1 = (\mathbf{q}\mathbf{r} - \mathbf{m}^2)\mathbf{p} + (\mathbf{p}\mathbf{t} - \mathbf{n}^2)\mathbf{q} > 0, \quad (11)$$

$$\mathbf{c}_2 = \mathbf{r}\mathbf{t} - \mathbf{p}\mathbf{q}, \quad (12)$$

$$\mathbf{c}_3 = -(\mathbf{r} + \mathbf{t}) < 0. \quad (13)$$

To simplify the quartic polynomial, we introduce the shift $\lambda = u + \frac{\mathbf{r}+\mathbf{t}}{4}$, which eliminates the cubic term and leads to the depressed quartic equation

$$u^4 + a_2 u^2 + a_1 u + a_0 = 0, \quad (14)$$

with

$$a_0 = -3 \frac{\mathbf{c}_3^4}{4^4} + \frac{\mathbf{c}_2 \mathbf{c}_3^2}{4^2} - \frac{\mathbf{c}_1 \mathbf{c}_3}{4} + \mathbf{c}_0,$$

$$a_1 = \frac{\mathbf{c}_3^3}{2^3} - \frac{\mathbf{c}_2 \mathbf{c}_3}{2} + \mathbf{c}_1,$$

$$a_2 = -3 \frac{\mathbf{c}_3^2}{8} + \mathbf{c}_2 < 0.$$

The four roots of the quartic polynomial can then be written in analytic form as

$$\lambda_1 = \frac{\mathbf{r} + \mathbf{t}}{4} + \frac{\sqrt{2y - a_2} + \sqrt{-2y - a_2 - \frac{2a_1}{\sqrt{2y - a_2}}}}{2}, \quad (15)$$

$$\lambda_2 = \frac{\mathbf{r} + \mathbf{t}}{4} + \frac{\sqrt{2y - a_2} - \sqrt{-2y - a_2 - \frac{2a_1}{\sqrt{2y - a_2}}}}{2}, \quad (16)$$

$$\lambda_3 = \frac{\mathbf{r} + \mathbf{t}}{4} - \frac{\sqrt{2y - a_2} - \sqrt{-2y - a_2 + \frac{2a_1}{\sqrt{2y - a_2}}}}{2}, \quad (17)$$

$$\lambda_4 = \frac{\mathbf{r} + \mathbf{t}}{4} - \frac{\sqrt{2y - a_2} + \sqrt{-2y - a_2 + \frac{2a_1}{\sqrt{2y - a_2}}}}{2}, \quad (18)$$

where the y is choosing for conveniency as

$$y = 2\sqrt{Q} \cos\left(\frac{1}{3} \arccos\left(\frac{R}{\sqrt{Q^3}}\right)\right) + \frac{a_2}{6}, \quad (19)$$

with

$$Q = \frac{a_2^2}{36} + \frac{a_0}{3}, \quad (20)$$

$$R = \frac{a_2^3}{216} - \frac{a_2 a_0}{6} + \frac{a_1^2}{16}. \quad (21)$$

It is worth noting that the largest eigenvalue λ_1 is always real and strictly positive. On the branch associated with the dominant Perron[33] eigenvalue, the second eigenvalue λ_2 is also real and satisfies $\lambda_1 > \lambda_2$, as demonstrated in Appendix A. The remaining eigenvalues λ_3 and λ_4 may be either real or form a complex-conjugate pair, depending on the Hamiltonian parameters. Moreover, no general ordering can be inferred for the magnitudes $|\lambda_2|$, $|\lambda_3|$, and $|\lambda_4|$, which may vary across parameter regimes (see Appendix A).

Among these, the largest eigenvalue can be identified as λ_1 . Thus in the thermodynamic limit, the free energy per unit cell is $f(T) = -k_B T \ln \lambda_1$, from which the entropy $\mathcal{S} = -\partial f / \partial T$, the specific heat $C = T \partial \mathcal{S} / \partial T$, and all other thermodynamic quantities follow in a standard way.

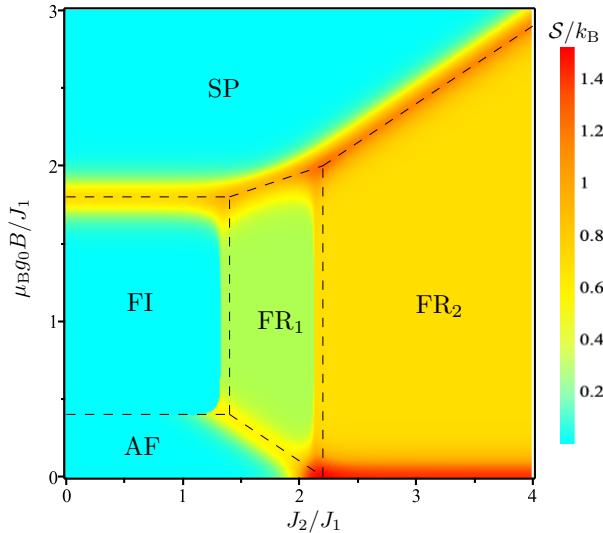


Figure 2: Zero-temperature phase diagram and low-temperature entropy density for the CTDC model. The phase diagram is shown in the $(J_2/J_1, B/J_1)$ plane for fixed $J_0 = -0.2$, and equal gyromagnetic factors $g_0 = g_1$, so that the Zeeman fields satisfy $h_0 = h_1 = g_0 \mu_B B$. The entropy plot at $k_B T/J_1 = 0.05$ displays the corresponding finite-temperature structure.

III. ZERO-TEMPERATURE PHASES AND PHASE DIAGRAM

We adopt the single-cell basis $|S_{a,k}, S_{b,k}; s_k\rangle$, with each spin variable $S_{a,k}, S_{b,k}, s_k = \pm \frac{1}{2}$. For a chain of N unit cells the Hamiltonian decomposes into local blocks, and the ground-state configurations of these blocks determine the zero-temperature phase diagram. Frustrated ground-state manifolds may exhibit extensive degeneracy, leading to a finite residual entropy $\mathcal{S}_0 \equiv \lim_{T \rightarrow 0} \mathcal{S}(T)$. At low but finite temperatures, this residual entropy manifests itself as nearly constant entropy plateaus. The low-temperature entropy map shown in Fig. 2 provides a direct visualization of this behavior: nonfrustrated regions appear in cyan, with vanishing entropy, while frustrated sectors form green and orange plateaus with $\mathcal{S}/k_B \simeq \frac{1}{2} \ln 2$ and $\mathcal{S}/k_B \simeq \ln 2$, respectively.

A. Ground states

For later comparison it is convenient to distinguish the sublattice polarizations $\langle s_k \rangle$, $\langle S_{a,k} \rangle = \langle S_{b,k} \rangle \equiv \langle S_k \rangle$, which varies between $-\frac{1}{2}$ and $\frac{1}{2}$, while the total magnetization per cell becomes $M = \mu_B (g_0 \langle s_k \rangle + 2g_1 \langle S_k \rangle)$.

1. Saturated phase (SP)

At sufficiently strong magnetic field the system becomes saturated phase (SP) or fully polarized

$$|\text{SP}\rangle = \bigotimes_{k=1}^N \left| \frac{1}{2}, \frac{1}{2}; \frac{1}{2} \right\rangle_k.$$

The energy per cell is

$$\varepsilon_{\text{SP}} = \frac{J_2}{4} + \frac{J_0 + 2J_1}{2} - \frac{2h_1 + h_0}{2}.$$

The local spin polarizations are $\langle s_k \rangle = \frac{1}{2}$ and $\langle S_k \rangle = \frac{1}{2}$, so the magnetization per cell is $M = \mu_B \frac{2g_1 + g_0}{2}$. Since the ground state is unique, the residual entropy vanishes, $\mathcal{S}_{\text{SP}} = 0$. In Fig. 2 the SP phase occupies the high-field plateaus, where the entropy drops to zero.

2. Partially frustrated phase

The frustrated phase (FR_1) has a period-two structure in which one cell is fully polarized, while the next remains locally frustrated. One representative configuration is

$$|\text{FR}_1\rangle = \bigotimes_{k=1}^{N/2} \left| \frac{1}{2}, \frac{1}{2}; \frac{1}{2} \right\rangle_{2k-1} \left| \eta_{2k}, -\eta_{2k}; -\frac{1}{2} \right\rangle_{2k}, \quad (22)$$

with $\eta_k = \pm \frac{1}{2}$, where every second dimer carries a free Ising orientation. Averaging over two consecutive cells gives the energy per cell

$$\varepsilon_{\text{FR}_1} = \frac{J_0}{4} - \frac{J_1}{2} - \frac{h_1}{2}. \quad (23)$$

The sublattice polarizations are $\langle S_k \rangle = \frac{1}{4}$ and $\langle s_k \rangle = 0$. The corresponding magnetization per cell is $M = \mu_B (g_0 \langle s_k \rangle + 2g_1 \langle S_k \rangle) = \mu_B \frac{g_1}{2}$. Because each frustrated cell carries one undetermined dimer orientation, and assuming an even number of unit cells, the ground state has $2^{N/2}$ configurations, which yields the residual entropy $\mathcal{S}/k_B = \frac{1}{2} \ln(2)$. In Fig. 2 this phase forms the intermediate-entropy plateau (green region) with $\mathcal{S}/k_B \simeq \frac{1}{2} \ln(2)$.

3. Fully frustrated phase

The second frustrated (FR_2) occurs when all nodal spins are polarized upward, $s_k = \frac{1}{2}$, while the dimer spins remain antiparallel. A convenient representative ground-state configuration is

$$|\text{FR}_2\rangle = \bigotimes_{k=1}^N \left| \eta_k, -\eta_k; \frac{1}{2} \right\rangle_k, \quad \eta_k = \pm \frac{1}{2}. \quad (24)$$

Inserting this configuration into the Eq.(1) yields the energy per cell

$$\varepsilon_{\text{FR}_2} = -\frac{J_2}{4} - \frac{h_0}{2}. \quad (25)$$

The dimer spin polarization vanishes, $\langle S_k \rangle = 0$, while the nodal sublattice is fully polarized, $\langle s_k \rangle = \frac{1}{2}$. The corresponding magnetization per cell is therefore $M = \mu_B \frac{g_0}{2}$.

Each dimer orientation $\eta_k = \pm \frac{1}{2}$ is independent, the ground-state degeneracy is 2^N , giving the residual entropy $\mathcal{S}_{\text{FR}_2}/k_B = \ln(2)$. In Fig.2, this phase corresponds to the high-entropy plateau (orange region), where the entropy reaches $\mathcal{S}/k_B \simeq \ln(2)$ at temperature $k_B T/J_1 = 0.05$.

4. Ferrimagnetic phase

The ferrimagnetic phase (FI) is characterized by fully polarized dimer spins and nodal spins aligned antiparallel to them. A representative configuration is

$$|\text{FI}\rangle = \bigotimes_{k=1}^N \left| \frac{1}{2}, \frac{1}{2}; -\frac{1}{2} \right\rangle_k. \quad (26)$$

The corresponding energy density is

$$\varepsilon_{\text{FI}} = \frac{J_2}{4} - \frac{J_0 + 2J_1}{2} - h_1 + \frac{h_0}{2}. \quad (27)$$

The sublattice spin polarizations are $\langle S_k \rangle = 1/2$, $\langle s_k \rangle = -1/2$. The corresponding physical magnetization per cell is $M = \mu_B \frac{2g_1 - g_0}{2}$. As the configuration is unique, the residual entropy vanishes, $\mathcal{S}_{\text{AF}} = 0$. In Fig. 2, the FI phase appears as the ordered region separating the AF and FR_1 sectors.

5. Antiferromagnetic phase

Finally, the antiferromagnetic (AF) phase exhibits a period-two alternation between fully polarized and fully reversed unit cells,

$$|\text{AF}\rangle = \bigotimes_{k=1}^{N/2} \left| \frac{1}{2}, \frac{1}{2}; \frac{1}{2} \right\rangle_{2k-1} \left| -\frac{1}{2}, -\frac{1}{2}; -\frac{1}{2} \right\rangle_{2k}. \quad (28)$$

with energy density given by

$$\varepsilon_{\text{AF}} = \frac{J_0}{2} - J_1 + \frac{J_2}{4}. \quad (29)$$

Since the spin contributions from the two sublattices cancel exactly, the nodal and dimer polarizations vanish, $\langle s_k \rangle = 0$ and $\langle S_k \rangle = 0$, while the total magnetization per cell is therefore $M = 0$. This configuration is unique up to global inversion, therefore the residual entropy is zero,

$\mathcal{S}_{\text{AF}}/k_B = 0$. In Fig. 2, the AF region appears immediately below the FI region, forming the low-entropy sector adjacent to the frustrated domains.

Taken together, the five phases SP, FI, AF, FR_1 , and FR_2 account for all ground-state regions observed in Fig. 2. The frustrated sectors produce the characteristic entropy plateaus, while the nondegenerate ordered regions is identified as low-entropy (cyan regions). Their boundaries constitute the zero-temperature skeleton underlying the sharp but continuous low-temperature crossovers discussed in the next subsection.

B. Phase boundary

The analytic phase boundaries for the symmetric-field case $g_0 = g_1$ follow from equating the corresponding ground-state energy densities and reproduce exactly the straight dashed lines observed in Fig. 2. Since $h_0 = h_1 = \mu_B g_0 B$, the phase diagram can be expressed directly in the $(J_2/J_1, \mu_B g_0 B/J_1)$ plane.

Two boundaries do not depend on J_2 and therefore appear as horizontal lines,

$$\begin{aligned} \text{FI} - \text{AF} : -h_1 + \frac{h_0}{2} &= J_0, & \mathcal{S}/k_B &= 0, \\ \text{FI} - \text{SP} : h_0 &= J_0 + 2J_1, & \mathcal{S}/k_B &= \ln(2), \end{aligned}$$

reflecting the fact that the competing phases have identical dependence on the intra-dimer coupling J_2 . The remaining boundaries have nonzero slope. They are

$$\begin{aligned} \text{FR}_1 - \text{AF} : h_0 &= \frac{-J_0 + 2J_1 - J_2}{2}, & \mathcal{S}/k_B &= \frac{1}{2} \ln(3), \\ \text{FR}_2 - \text{SP} : h_1 &= \frac{J_0}{2} + J_1 + \frac{J_2}{2}, & \mathcal{S}/k_B &= \ln(3), \end{aligned}$$

where in both cases the factor $\ln(3)$ arises because the competing configurations at the phase boundary generate an additional local degree of freedom not present in the bulk phases.

These lines are accompanied by a short slanted segment in the interval $J_2 \in [3J_0 + 2J_1, 2J_1 - J_0]$, given by

$$\text{FR}_1 - \text{SP} : h_0 + h_1 = \frac{J_2 + 6J_1 + J_0}{4}, \quad \mathcal{S}/k_B = \ln(2).$$

This segment corresponds precisely to the narrow oblique boundary clearly visible between the FI – FR_1 and FR_1 – FR_2 lines in Fig. 2.

Finally, there are two peculiar boundaries,

$$\begin{aligned} \text{FI} - \text{FR}_1 : h_1 - h_0 &= \frac{J_2 - 3J_0 - 2J_1}{2}, \\ \text{FR}_1 - \text{FR}_2 : h_1 - h_0 &= \frac{J_2 + J_0 - 2J_1}{2}, \end{aligned}$$

and these do not exhibit any enhancement of the boundary residual entropy. It is worth noting that both of these

boundaries produce clear pseudotransition signatures at low temperature. In Fig. 2 they manifest as sharp entropic ridges that separate the ordered and frustrated regions in the FI – FR₁ case, and similarly as a distinct ridge between the two frustrated states in the FR₁ – FR₂ case.

C. Nearly block-diagonal form of the transfer matrix

Since the transfer matrix \mathbf{V} given in Eq. (2) is irreducible, the Non-existence of phase transition theorem[33] guarantees the absence of true phase transitions. Nevertheless, \mathbf{V} may become nearly block diagonal in certain parameter regimes. In this case, the approach proposed in Ref. [34] provides a useful framework to analyze pseudocritical behavior from a general perspective, without this tool it would become a cumbersome task find the pseudocritical temperature. Following this approach, we reorganize the transfer matrix into a nearly block-diagonal form in order to identify the competing thermodynamic sectors responsible for the observed pseudocritical temperatures.

1. Pair-sector decomposition

The transfer matrix \mathbf{V} is written in the pair basis $\{|+\rangle, |+\rangle, |-\rangle, |-\rangle, |-\rangle, |-\rangle\}$, where each state labels two consecutive nodal spins (s_k, s_{k+1}).

This basis can be conveniently splits into two distinct sectors:

(i) Parallel sector $\{|+\rangle, |-\rangle\}$, corresponding to locally uniform spin configurations.

(ii) Antiparallel sector $\{|+\rangle, |-\rangle\}$, corresponding to locally alternating nodal spin configurations.

In terms of the ground-state patterns discussed above, the FR₂ and FI manifolds are predominantly supported on parallel sector, whereas the FR₁ manifold is supported on antiparallel sector. Consequently, the FI – FR₁ and FR₁ – FR₂ pseudotransitions can be viewed as successive competitions between these two pair sectors.

2. Nearly block-diagonal structure of the transfer matrix

Reordering the pair basis as $\{|+\rangle, |-\rangle\} \oplus \{|+\rangle, |-\rangle\}$, the transfer matrix can be written in the block form

$$\mathbf{V} = \begin{pmatrix} \mathbf{A} & \mathbf{C} \\ \mathbf{D} & \mathbf{B} \end{pmatrix}, \quad (30)$$

where the diagonal blocks are given by

$$\mathbf{A} = \begin{pmatrix} \mathfrak{r} & 0 \\ 0 & \mathfrak{t} \end{pmatrix}, \quad \mathbf{B} = \begin{pmatrix} 0 & \mathfrak{p} \\ \mathfrak{q} & 0 \end{pmatrix}, \quad (31)$$

and the off diagonal blocks read

$$\mathbf{C} = \begin{pmatrix} \mathfrak{m} & 0 \\ 0 & \mathfrak{n} \end{pmatrix}, \quad \mathbf{D} = \begin{pmatrix} 0 & \mathfrak{n} \\ \mathfrak{m} & 0 \end{pmatrix}. \quad (32)$$

The diagonal blocks \mathbf{A} and \mathbf{B} propagate configurations within the parallel and antiparallel sectors, respectively, while the off-block matrices \mathbf{C} and \mathbf{D} encode processes that convert one sector into the other, which may be interpreted as domain-wall-like events.

Although \mathbf{V} is irreducible, the inter-sector couplings \mathbf{C} and \mathbf{D} can become parametrically small in the low-temperature regime. In this sense, the transfer matrix is nearly block diagonal: the dominant statistical weight is carried by one sector at a time, and pseudocritical behavior emerges when the leading eigenvalues associated with different sectors become nearly degenerate. This nearly reducible structure provides the spectral mechanism underlying the sharp yet analytic crossovers discussed in the main text.

The eigenvalues of the block \mathbf{A} are trivially $\lambda = \{\mathfrak{r}, \mathfrak{t}\}$, while the eigenvalues of the block \mathbf{B} are $\lambda = \pm\sqrt{\mathfrak{p}\mathfrak{q}}$.

3. Pseudocritical temperature

According to the criterion discussed in Ref. [34], pseudocritical behavior arises when the transfer matrix acquires a nearly block-diagonal structure, such that the leading eigenvalues associated with competing blocks become comparable. In the present case, this leads to two possible pseudocritical conditions, depending on which eigenvalue of the block \mathbf{A} is dominant:

$$\mathfrak{t} = \sqrt{\mathfrak{p}\mathfrak{q}} \Rightarrow T_{p_1} : \text{ associated to FR}_1 - \text{FI}, \quad (33)$$

$$\mathfrak{r} = \sqrt{\mathfrak{p}\mathfrak{q}} \Rightarrow T_{p_2} : \text{ associated to FR}_2 - \text{FI}. \quad (34)$$

These relations provide a transparent interpretation of the two pseudocritical temperature scales observed in the thermodynamic analysis. It is worth emphasizing that they follow directly from the criterion of Ref. [34]. Although simple in form, the resulting conditions involve transcendental equations.

Alternatively, the pseudocritical temperature T_p can also be determined along any fixed parameter cut in the low-temperature regime. For instance at fixed J_0, J_1, J_2 , while varying B , follows from the crossing of the low temperature free energy branches of the two competing phases. Approximating each free energy by $f_A(T) \simeq \varepsilon_A - k_B T s_A$, the condition $f_A(T_p) = f_B(T_p)$ yields the standard estimate of pseudocritical temperature

$$k_B T_p \approx \frac{\varepsilon_B - \varepsilon_A}{S_B - S_A}. \quad (35)$$

Applying this expression to the competition between FI and FR₁ gives

$$T_{p_1} \approx \frac{3J_0 + 2J_1 - J_2 + 2(h_1 - h_0)}{2k_B \ln(2)}, \quad (36)$$

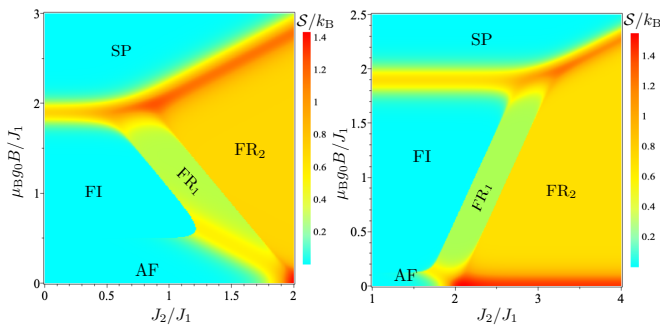


Figure 3: Low-temperature phase diagram of the CTDC for $g_0 \neq g_1$ under a uniform external field B , assuming fixed $J_0/J_1 = -0.1$. (left) Dimer spins have weaker Zeeman response, $g_1/g_0 = 0.7$. (right) Dimer spins have stronger Zeeman response, $g_1/g_0 = 1.3$. The entropy plot at $k_B T/J_1 = 0.05$ displays the corresponding finite-temperature structure.

which accurately reproduces the low-temperature behavior of T_{p_1} obtained in Eq. (33). In a similarly manner, the pseudocritical temperature associated with the FR_1 and FR_2 competition is estimated as

$$T_{p_2} \approx \frac{2J_1 - J_0 - J_2 + 2(h_1 - h_0)}{2k_B \ln(2)}. \quad (37)$$

in good agreement with Eq. (34) in the low temperature region.

Both expressions vanish linearly as the parameters approach their respective zero-temperature boundaries. If $g_0 = g_1$, T_{p_1} and T_{p_2} are independent of B , and appears as vertical lines in Fig.2.

In Fig. 3 is shown, how the low-temperature entropy $S(T)$ landscape changes in the $(J_2/J_1, \mu_B g_0 B/J_1)$ plane, when the two sublattices have $g_0 \neq g_1$. In panel (left), where $g_1/g_0 > 1$, the frustrated boundaries that appear as vertical lines in the symmetric case tilt into straight lines with a positive slope. In panel (right), where $g_1/g_0 < 1$, the same boundaries acquire a negative slope, producing an opposite deformation of the diagram.

Although the geometric orientation of the boundaries changes, the entropy plateaus remain unchanged: the ordered phases occupy the low-entropy cyan regions, while the frustrated FR_1 and FR_2 exhibit green and orange regions characteristic values $S/k_B = \frac{1}{2} \ln(2)$ and $\ln(2)$, respectively. The $FR_1 - SP$ oblique boundary also persists as a distinct entropic ridge in both panels, although shifted and tilted by the asymmetric Zeeman response.

Importantly, the deformation of these boundaries does not suppress the thermal anomalies associated with the frustrated manifold. The tilted ridges that separate FI from FR_1 , and FR_1 from FR_2 continue to generate clear pseudotransition signatures at low temperature, reflected in the sharp entropic gradients that survive in both panels.

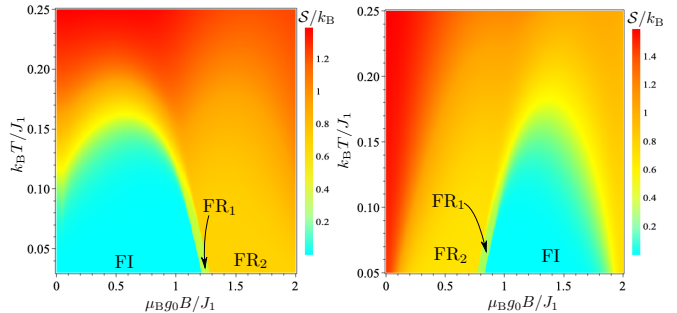


Figure 4: Density plot of the entropy in the $(\mu_B g_0 B/J_1, k_B T/J_1)$ plane, for a weak ferromagnetic coupling J_0 . (left) $J_0/J_1 = -0.01$, $J_2/J_1 = 1.2$ and $g_1/g_0 = 0.7$; (right) Similarly for $J_0/J_1 = -0.01$, $J_2/J_1 = 2.4$ and $g_1/g_0 = 1.3$.

IV. THERMODYNAMICS AND PSEUDOTRANSITION

Here we examine the thermodynamic and magnetic properties in the vicinity of the anomalous crossover.

A. Entropy and specific heat

In Fig. 4 is reported the low-temperature entropy landscape in the $(\mu_B g_0 B/J_1, k_B T/J_1)$ plane for $g_1 \neq g_0$. Panel (left), obtained for $J_0/J_1 = -0.01$, $J_2/J_1 = 1.2$ and $g_1/g_0 = 0.7$, shows three distinct low-temperature domains that reproduce the structure of the ground-state phase diagram. A narrow green plateau associated with the FR_1 phase appears between the FI and FR_2 sectors, and its boundary acquires a negative slope due to the asymmetric Zeeman response. In this region the entropy ridges separating the ordered and frustrated sectors mark the emergence of two pseudotransition scales, one related to the competition between FI and FR_1 and another associated with the competition between FR_1 and FR_2 . These features become progressively smoother as the temperature increases. Panel (right), corresponding to $J_0/J_1 = -0.01$, $J_2/J_1 = 2.4$ and $g_1/g_0 = 1.3$, shows the opposite situation where the frustrated boundaries tilt with positive slope, reflecting the opposite imbalance in the magnetic response. The pseudotransition ridges remain visible, indicating that the entropic signatures of the frustrated manifold are robust against variations in the ratio g_1/g_0 .

Figure 5 shows the temperature dependence of the entropy and specific heat for two representative parameter sets reported in the caption of Fig.5, illustrating the emergence of two distinct pseudocritical temperatures. These scales are associated with the FI to FR_1 crossover, with pseudocritical temperature given by Eq.(33) at $k_B T_{p_1}/J_1 \approx 0.0504764$, and with the FR_1 to FR_2 crossover, with pseudocritical temperature given by Eq. (34) at $k_B T_{p_2}/J_1 \approx 0.0788948$. Panels (a) and

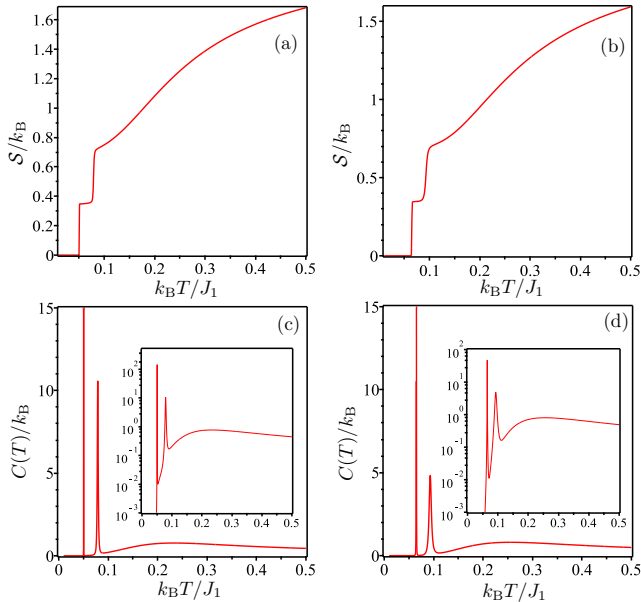


Figure 5: (a) Entropy as functions of temperature for $J_2/J_1 = 1.24$, $J_0/J_1 = -0.01$, $\mu_B g_0 B/J_1 = 1.1$, and $g_1/g_0 = 0.7$. (b) Entropy as functions of temperature for $J_2/J_1 = 2.48$, $J_0/J_1 = -0.01$, $\mu_B g_0 B/J_1 = 1$, and $g_1/g_0 = 1.3$. (c) Specific heat for the parameters in panel (a), with an inset showing $C(T)$ on a logarithmic temperature scale. (d) Specific heat for the parameters in panel (b), with an inset showing $C(T)$ on a logarithmic temperature scale.

(b) display the entropy curves, which show two smooth but clearly separated increases as temperature rises. The lower increase at T_{p_1} corresponds to the partial activation of the FR₁ manifold, whereas the higher increase at T_{p_2} signals access to the fully frustrated FR₂ sector.

Panels (c) and (d) present the corresponding specific heat $C(T)$, which develops two continuous maxima at T_{p_1} and T_{p_2} . The logarithmic insets make the locations of these maxima particularly visible. The first maximum marks the crossover between the ordered FI region and the partially frustrated FR₁ configurations, while the second reflects the competition between FR₁ and FR₂. We can observe that the peak at T_{p_1} is higher and sharper than the second peak at T_{p_2} . This behavior is consistent with the pseudocritical features reported in the literature [4, 6, 12, 13].

The clear separation between these double thermal anomalies shows that the model supports two well defined pseudocritical temperature scales, each associated with a distinct degeneracy change in the ground-state structure.

B. Magnetic properties

Figure 6 shows the temperature dependence of the magnetization, the sublattice averages, and the magnetic susceptibility for the same parameter sets used in Fig. 5.

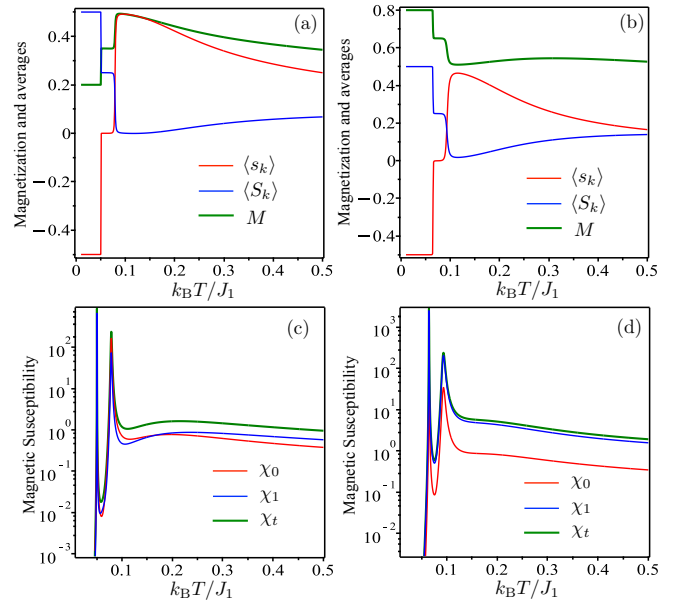


Figure 6: Magnetization (M) and averages $\langle s_k \rangle$ and $\langle S_k \rangle$, as functions of temperature. (a) For $J_2/J_1 = 1.24$, $J_0/J_1 = -0.01$, $\mu_B g_0 B/J_1 = 1.1$, and $g_1/g_0 = 0.7$. (b) For $J_2/J_1 = 2.48$, $J_0/J_1 = -0.01$, $\mu_B g_0 B/J_1 = 1$, and $g_1/g_0 = 1.3$. (c) Magnetic susceptibility for the parameters in panel (a). (d) Magnetic susceptibility for the parameters in panel (b).

Panels (a) and (b) display $\langle s_k \rangle$, $\langle S_k \rangle$ and M as functions of temperature. All three curves show two smooth but clearly separated steps. The first step, located at the pseudocritical temperature T_{p_1} , reflects the partial activation of the FR₁ configurations, which introduce local frustration while keeping the nodal subsystem partially aligned. The second step, located at T_{p_2} , marks the activation of the fully frustrated FR₂ manifold, where each dimer contributes an additional independent degree of freedom.

The dimer and nodal magnetic susceptibilities are defined through the derivative of the free energy with respect to the external field B , namely $\chi_0(T) = \mu_B g_0 \frac{\partial \langle s_k \rangle}{\partial B}$, $\chi_1(T) = 2\mu_B g_1 \frac{\partial \langle S_k \rangle}{\partial B}$, whereas the total magnetic susceptibility is $\chi_t(T) = \chi_0(T) + \chi_1(T)$.

Panels (c) and (d) of Fig. 6 show χ_0 , χ_1 , and χ_t on a logarithmic scale. All three susceptibilities develop two pronounced peaks at T_{p_1} and T_{p_2} . These peaks coincide with the pseudocritical temperatures identified from the entropy and specific-heat analysis. Although the peaks appear sharp, they remain finite and represent the typical thermal signatures of pseudotransitions in frustrated one-dimensional systems. Again, the anomalies occur at the same temperatures identified from the entropy and specific heat, and the peak at T_{p_1} is higher and sharper than the one at T_{p_2} . This confirms the consistency of the dual pseudotransition behavior in the CTDC model.

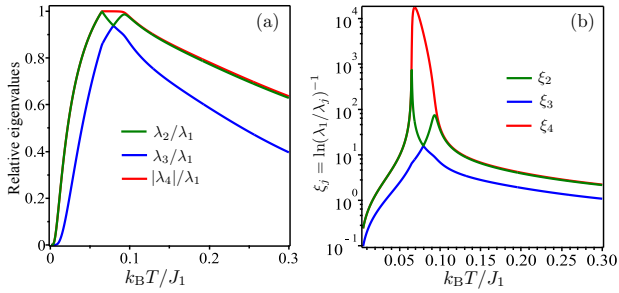


Figure 7: (a) Temperature dependence of the relative eigenvalues $|\lambda_j|/\lambda_1$ for the fixed parameters $J_2/J_1 = 2.48$, $J_0/J_1 = -0.01$, $\mu_B g_0 B/J_1 = 1$, and $g_1/g_0 = 1.3$. (b) Temperature dependence of the quantities $\xi_j = \ln(\lambda_1/|\lambda_j|)^{-1}$ for the same set of parameters as in panel (a).

C. Eigenvalues properties and correlation length

Figure 9(a) shows the temperature dependence of the relative eigenvalues $|\lambda_j|/\lambda_1$ for the parameter set $J_2/J_1 = 1.24$, $J_0/J_1 = -0.01$, $\mu_B g_0 B/J_1 = 1.1$, and $g_1/g_0 = 0.7$. Although the eigenvalues satisfy the ordering $\lambda_1 > \lambda_2 > \lambda_3 > \lambda_4$, the subleading eigenvalue in modulus is not λ_2 but rather $|\lambda_4|$ (see appendix A). This behavior is illustrated by the red curve $|\lambda_4|/\lambda_1$, while the green and blue curves correspond to λ_2/λ_1 and λ_3/λ_1 , respectively. The ratio $|\lambda_4|/\lambda_1$ exhibits a broad plateau between the two pseudocritical temperatures, indicating that the same low-energy sector remains dominant throughout this interval. In contrast, the ratio λ_2/λ_1 displays two pronounced extrema located precisely at the pseudocritical temperatures T_{p_1} and T_{p_2} , reflecting the successive competition between distinct thermodynamic sectors.

For the same parameters, Fig. 9(b) shows the quantities $\xi_j = [\ln(\lambda_1/|\lambda_j|)]^{-1}$ as functions of temperature on a logarithmic scale. Since $|\lambda_4|$ is the largest subleading eigenvalue in modulus, the spectral correlation length is given by $\xi = \xi_4 = [\ln(\lambda_1/|\lambda_4|)]^{-1}$. However, this quantity does not exhibit signatures of the pseudocritical behavior. By contrast, the quantity $\xi_2 = [\ln(\lambda_1/\lambda_2)]^{-1}$, although not a correlation length in the strict spectral sense, clearly signals both pseudocritical temperatures T_{p_1} and T_{p_2} . In general, the spectral correlation length is determined by

$$\xi = \left[\ln \left(\frac{\lambda_1}{\max\{|\lambda_2|, |\lambda_3|, |\lambda_4|\}} \right) \right]^{-1}, \quad (38)$$

whereas pseudocritical behavior is associated with near-degeneracies between the leading eigenvalues that govern the dominant thermodynamic sectors.

Although universality and quasicritical exponents have been identified for a broad class of one-dimensional decorated models [6], a quantitative scaling analysis of correlation lengths is not pursued here. In contrast, the

quantity $\xi_2 = [\ln(\lambda_1/\lambda_2)]^{-1}$ exhibits anomalous critical behavior, but a detailed analysis of its associated exponents lies beyond the scope of the present work.

The emergence of two pseudocritical temperatures in the present model is closely related to the coupling of two diamond units within the same chain. However, increasing the number of diamond units or coupling additional chains does not, in general, guarantee the appearance of further pseudocritical temperatures. In the coupled twin-diamond chain, the internal structure of the unit cell supports two frustrated manifolds, FR_1 and FR_2 , with different extensive degeneracies, leading to successive entropy-driven free-energy crossings as temperature increases and hence to two well-separated pseudotransitions. Additional pseudotransitions may arise only when the enlarged unit cell stabilizes new competing low-energy sectors with distinct residual entropies that survive the coupling, consistently with the criterion discussed in Ref. [11].

V. CONCLUSION

In this work we have presented an exact analysis of the coupled twin-diamond chain (CTDC), a decorated one-dimensional Ising system inspired by the magnetic structure of $\text{Cu}_2(\text{TeO}_3)_2\text{Br}_2$. The model contains two inequivalent sublattices, allowing for distinct local fields, and includes three exchange couplings that control the interplay between nodal spins and internal dimers. Using the star-triangle mapping[29–31] and the resulting 4×4 transfer matrix, we obtained analytic expressions for the eigenvalues governing the full thermodynamics of the system.

The zero-temperature analysis reveals five distinct ground-state sectors: the saturated phase (SP), the ferrimagnetic phase (FI), the antiferromagnetic phase (AF), and two frustrated phases, FR_1 and FR_2 . Each phase is characterized by a simple product state, and their energy densities, sublattice polarizations, and residual entropies were derived explicitly. The two frustrated phases carry extensive degeneracies, yielding residual entropies $\mathcal{S}/k_B = \frac{1}{2} \ln(2)$ for FR_1 and $\mathcal{S}/k_B = \ln(2)$ for FR_2 . These values are directly reflected in the low-temperature entropy map, where FR_1 and FR_2 induce the intermediate- and high-entropy plateaus regions, respectively.

The complete phase diagram in the $(J_2/J_1, \mu_B g_0 B/J_1)$ plane shows that the frustrated sectors occupy extended regions between the ordered phases. Because the boundaries between these sectors involve ground-state level crossings accompanied by changes in degeneracy, the associated finite-temperature behavior displays sharp but continuous features. In particular, the entropy and magnetization exhibit steplike but nondiscontinuous variations, while the specific heat and susceptibility develop pronounced finite peaks-typical signatures of pseudotransition behavior previously reported for other decorated Ising chains.

Altogether, the CTDC provides another exactly solvable example in which competing local configurations and internal degeneracies generate well-defined frustrated regions and clear thermodynamic precursors of pseudotransitions at low temperature. The analytic structure offers a clear framework for understanding how decoration, sublattice asymmetry, and frustration generate dual pseudocritical scales in the CTDC model.

Appendix A: Pairwise structure of the eigenvalues

Here we clarify the algebraic structure of the four eigenvalues of the transfer matrix and show that two eigenvalues associated with the Perron branch, namely λ_1 and λ_2 given in Eqs. (15) and (16), are necessarily real, while the remaining eigenvalues may be either real or form a complex-conjugate pair.

1. Pairwise algebraic structure of the spectrum

The exact diagonalization yields the four eigenvalues in the form

$$\lambda_1 = c + \frac{R_1 + \sqrt{R_-}}{2}, \quad \lambda_2 = c + \frac{R_1 - \sqrt{R_-}}{2}, \quad (\text{A1})$$

$$\lambda_3 = c - \frac{R_1 - \sqrt{R_+}}{2}, \quad \lambda_4 = c - \frac{R_1 + \sqrt{R_+}}{2}, \quad (\text{A2})$$

with

$$c = \frac{\tau + t}{4}, \quad R_1 = \sqrt{2y - a_2}, \quad (\text{A3})$$

and

$$R_{\mp} = -2y - a_2 \mp \frac{2a_1}{R_1}. \quad (\text{A4})$$

Here all coefficients are real, and the auxiliary variable y is chosen as a real root of the resolvent cubic.

Equation (A1) shows that the spectrum naturally decomposes into two algebraic pairs: (λ_1, λ_2) , controlled by the radicand R_- , and (λ_3, λ_4) , controlled by R_+ . Any complex eigenvalues can therefore arise only within one of these pairs.

2. Reality of λ_1 and λ_2

The transfer matrix has strictly positive entries and is primitive. By the Perron-Frobenius theorem [33], the dominant eigenvalue λ_1 is real, strictly positive, and non-degenerate, and is given by the first expression in Eq. (A1). If $R_- < 0$, then $\sqrt{R_-}$ would be purely imaginary, causing λ_1 to acquire a nonzero imaginary part, which is impossible. Therefore $R_- \geq 0$, and both λ_1 and λ_2 are real on the thermodynamic branch.

3. Remaining eigenvalues and possible complex conjugate pair

No analogous restriction applies to the second radicand R_+ . If $R_+ < 0$, then $\sqrt{R_+}$ is purely imaginary, and Eq. (A1) immediately yields $\lambda_4 = \lambda_3^*$, so that λ_3 and λ_4 form a complex-conjugate pair. If $R_+ \geq 0$, all four eigenvalues are real.

Thus, on the thermodynamic branch, the spectrum always contains at least two real eigenvalues, λ_1 and λ_2 , while the remaining pair may be real or complex conjugate, depending on the Hamiltonian parameters.

4. Magnitude of eigenvalues

Although the eigenvalues λ_j are labeled according to their algebraic expressions, their ordering on the real axis is parameter dependent. Even when all eigenvalues are real, the second-largest eigenvalue in magnitude need not coincide with λ_2 ; depending on parameters, it may instead correspond to λ_3 or λ_4 . Consequently, subleading behavior is governed by the eigenvalue with the largest modulus among $\lambda_{j \neq 1}$, rather than by a fixed algebraic branch.

Acknowledgments

This work was partially supported by the Brazilian agencies CNPq and FAPEMIG.

-
- [1] L. Galisova and J. Strečka, Vigorous thermal excitations in a double-tetrahedral chain of localized Ising spins and mobile electrons mimic a temperature-driven first-order phase transition, *Phys. Rev. E* **91**, 022134 (2015) I
 [2] J. Strecka, R. C. Alecio, M. Lyra, and O. Rojas, Spin frustration of a spin-1/2 Ising-Heisenberg three-leg tube as an indispensable ground for thermal entanglement, *J. Magn. Magn. Mater.* **409**, 124 (2016) I
 [3] O. Rojas, J. Strecka, S.M. de Souza, Thermal entangle-

- ment and sharp specific-heat peak in an exactly solved spin-1/2 Ising-Heisenberg ladder with alternating Ising and Heisenberg inter-leg couplings, *Solid St. Commun.* **246**, 68 (2016). I
 [4] S. M. de Souza, O. Rojas, Quasi-phases and pseudotransitions in one-dimensional models with nearest neighbor interactions, *Sol. Stat. Comm.* **269**, 131 (2018) I, IV A
 [5] I.M. Carvalho, J. Torrico, S.M. de Souza, O. Rojas, O.

- Derzhko, Correlation functions for a spin-1/2 Ising-XYZ diamond chain: Further evidence for quasi-phases and pseudo-transitions, *Ann. Phys.* **402**, 45 (2019). I
- [6] O. Rojas, J. Strečka, M. L. Lyra, and S. M. de Souza, Universality and Quasicritical Exponents of One-Dimensional Models Displaying a Quasitransition at Finite Temperatures, *Phys. Rev. E* **99**, 042117 (2019). I, IV A, IV C
- [7] O. Rojas, J. Strečka, O. Derzhko, and S. M. de Souza, Peculiarities in pseudo-transitions of a mixed spin-(1/2,1) Ising-Heisenberg double-tetrahedral chain in an external magnetic field, *J. Phys.: Condens. Matter* **32**, 035804 (2019). I
- [8] Y. Panov and O. Rojas, Zero temperature phase transitions and their anomalous influence on thermodynamic behavior in the q -state Potts model on a diamond chain, *Phys. Rev. E* **108**, 044144 (2023)
- [9] T. Krokhmalkii, T. Hutak, O. Rojas, S. M. de Souza, and O. Derzhko, Towards low-temperature peculiarities of thermodynamic quantities for decorated spin chains, *Physica A* **573**, 125986 (2021).
- [10] J. Chapman B. Tomasello and S. Carr, Bifurcation in correlation length of the Ising model on a ‘Toblerone’ lattice, *J. Stat. Mech.* 093214 (2024) I
- [11] O. Rojas, A conjecture on the relationship between critical residual entropy and finite temperature pseudo-transitions of one-dimensional models, *Braz. J. Phys.* **50**, 675 (2020). I, IV C
- [12] O. Rojas, S. M. de Souza, J. Torrico, L. M. Veríssimo, M. S. S. Pereira, M. L. Lyra, and O. Derzhko, Unusual low-temperature behavior in the half-filled band of the one-dimensional extended Hubbard model in atomic limit, *Phys. Rev. E* **110**, 024130 (2024). I, IV A
- [13] J. Strečka and K. Karlova, Pseudo-transition between antiferromagnetic and charge orders in a minimal spin-pseudospin model of one-dimensional cuprates, *Eur. Phys. J. B* **97**, 74 (2024). I, IV A
- [14] Y. Panov and O. Rojas, Unconventional Low Temperature Features in the One-Dimensional Frustrated q -State Potts Model, *Phys. Rev. E* **103**, 062107 (2021). I
- [15] D. Yasinskaya and Y. Panov, Pseudotransitions in a dilute Ising chain, *Phys. Rev. E* **110**, 044118 (2024) I
- [16] F. F. Braz S. M. de Souza, M. L. Lyra, O. Rojas, Thermodynamic constraints and pseudotransition behavior in a one-dimensional waterlike system, *Phys. Rev. E* **112**, 044144 (2025) I
- [17] J. Strečka, Anomalous Thermodynamic Response in the Vicinity of a Pseudo-Transition of a Spin-1/2 Ising Diamond Chain, *Acta Phys. Pol. A* **137**, 610 (2020) I
- [18] L. Čanová, J. Strečka, and M. Jaščur, Exact results of the Ising-Heisenberg model on the diamond chain with spin-1/2, *Czech. J. Phys.*, **54** (S4), 579 (2004).
- [19] J. Strečka, T. Verkholyak, J. Richter, K. Karlova, O. Derzhko, J. Schnack, Frustrated magnetism of spin-1/2 Heisenberg diamond and octahedral chains as a statistical-mechanical monomer-dimer problem, *Phys. Rev. B* **105** (2022) 064420 I
- [20] H. Kikuchi, Y. Fujii, M. Chiba, S. Mitsudo, T. Idehara, Magnetic properties of the frustrated diamond chain compound $\text{Cu}_3(\text{CO}_3)_2(\text{OH})_2$, *Physica B*, **329**, 967 (2003). I
- [21] H. Kikuchi, Y. Fujii, M. Chiba, S. Mitsudo, T. Idehara, T. Kuwai, Experimental evidence of the one-third magnetization plateau in the diamond chain compound $\text{Cu}_3(\text{CO}_3)_2(\text{OH})_2$, *J. Mag. Mag. Mat.* **272**, 900 (2004) I
- [22] M. Sorolla, X. Wang, L. Kubířková, V. Ksenofontov, A. Möller, A. J. Jacobson, A Mixed-Valent Iron (II/III) Diamond Chain with Single-Ion Anisotropy, *Inorg. Chem.* **59**, 1068 (2020) I
- [23] H. A. Zad, N. Ananikian and R. Kenna, The specific heat and magnetic properties of two species of spin-1/2 ladders with butterfly-shaped unit blocks, *J. Phys.: Condens. Matter* **31**, 445802 (2019) I
- [24] L. Chakhmakhchyan, N. Ananikyan, L. Ananikyan and C. Burdik, Thermal entanglement of the spin-1/2 diamond chain, *J. Phys.: Conf. Ser.* **343**, 012022 (2012) I
- [25] D. Uematsu and M. Sato, Magnetic Properties of $\text{Cu}_3(\text{TeO}_3)_2\text{Br}_2$ with Spin 1/2 Diamond Lattice, *J. Phys. Soc. Jap.*, **76**, 084712 (2007) I, II
- [26] D. C. Kakarla et al., Exploring new members of magnetoelectric materials in $\text{CuO-CuCl}_2\text{-SeO}_2$ system, *Mat. Tod. Phys.* **46**, 101527 (2022) I
- [27] W. Lafargue-Dit-Hauret and X. Rocquefelte, Unveiling electronic and magnetic properties of $\text{Cu}_3(\text{SeO}_3)_2\text{Cl}_2$ and $\text{Cu}_3(\text{TeO}_3)_2\text{Br}_2$ oxohalide systems via first-principles calculations, *J. Phys.: Condens. Matter* **34**, 095802 (2022) I
- [28] A. F. Murtazoev et al., Cadmium copper selenite chloride, $\text{CdCu}_2(\text{SeO}_3)_2\text{Cl}_2$, an insulating spin gap system, *Jour. Sol. Stat. Chem.*, **303**, 122518 (2021) I
- [29] O. Rojas, J.S. Valverde, S.M. de Souza, Generalized transformation for decorated spin models, *Physica A* **388**, 1419 (2009) II A, V
- [30] O. Rojas, S. M. de Souza, Direct algebraic mapping transformation for decorated spin models, *J. Phys. A: Math. Theor.* **44**, 245001 (2011)
- [31] J. Strečka, Generalized algebraic transformations and exactly solvable classical-quantum models, *Phys. Lett. A*, **374**, 3718 (2010) II A, V
- [32] J. Stephenson, Two one-dimensional Ising models with disorder points, *Can. J. Phys.* **48**, 1724 (1970). II A
- [33] J. A. Cuesta and A. Sanchez, General Non-Existence Theorem for Phase Transitions in One-Dimensional Systems with Short Range Interactions, and Physical Examples of Such Transitions, *J. Stat. Phys.* **115**, 869 (2003) II A, III C, A 2
- [34] O. Rojas, Spectral mechanism and nearly reducible transfer matrices for pseudotransitions in one-dimensional systems, *Physica A* **685**, 131295 (2026). III C, III C 3, III C 3